

Spin filtering with insulating altermagnets

Kartik Samanta^{1,*}, Ding-Fu Shao^{2,†}, and Evgeny Y. Tsymbal^{1,‡}

¹ *Department of Physics and Astronomy & Nebraska Center for Materials and Nanoscience, University of Nebraska, Lincoln, Nebraska 68588-0299, USA*

² *Key Laboratory of Materials Physics, Institute of Solid-State Physics, HFIPS, Chinese Academy of Sciences, Hefei 230031, China*

Altermagnetic (AM) materials have recently attracted significant interest due to the non-relativistic momentum-dependent spin splitting of their electronic band structure which may be useful for antiferromagnetic (AFM) spintronics. So far, however, most research studies have been focused on AM *metals* which can be utilized in spintronic devices, such as AFM tunnel junctions (AFMTJs). At the same time, AM *insulators* have remained largely unexplored in the realm of AFM spintronics. Here, we propose to employ AM insulators (AMIs) as efficient spin-filter materials. By analyzing the complex band structure of rutile-type altermagnets MF_2 ($M = \text{Fe, Co, Ni}$), we demonstrate that the evanescent states in these AMIs exhibit spin- and momentum-dependent decay rates resulting in a substantial momentum-dependent spin polarization of the tunneling current. Using a model of spin-filter tunneling across a spin-dependent potential barrier, we estimate the TMR effect in spin-filter magnetic tunnel junctions (SF-MTJs) that include two magnetically decoupled MF_2 (001) barrier layers. We predict a sizable spin-filter TMR ratio of about 150-170% in SF-MTJs based on AMIs CoF_2 and NiF_2 if the Fermi energy is tuned to be close to the valence band maximum. Our results demonstrate that AMIs provide a viable alternative to conventional ferromagnetic or ferrimagnetic spin-filter materials, potentially advancing the development of next-generation AFM spintronic devices.

The field of spintronics exploits the spin degree of freedom in solid-state electronic devices for information processing and storage [1]. Spintronics relies on electric currents carrying spin polarization that is used to detect or control the magnetic order parameter. Obtaining a sizable spin polarization is therefore an important aspect of spintronics. One of the promising approaches to generate highly spin-polarized electric currents is to employ spin-filter tunneling, where a spin-filter material, typically a ferromagnetic (FM) insulator, is used as a barrier in a spin-filter magnetic tunnel junction (SF-MTJ) [2]. Spin-filter tunneling is considered as a viable alternative to a more conventional approach based on magnetic tunnel junctions (MTJs) which utilize the magnetic alignment of two FM electrodes to produce a tunneling magnetoresistance (TMR) effect [3-8].

Electron tunneling through an insulating layer can be understood in terms of evanescent states which represent the eigen-states of the insulator within its energy band gap [9]. Their wave-functions decay exponentially with a rate κ that is determined by the complex band structure of the insulator [10-12]. In FM insulators, the exchange splitting of the spin bands leads to a spin-dependent tunneling barrier and hence spin-dependent decay rates. As tunneling transmission depends exponentially on the decay rate, electrons are transmitted with significantly different probabilities depending on their spin orientation, resulting in tunneling spin polarization [13]. This represents the basic idea of spin-filter tunneling.

A Tedrow-Meservey technique of spin-polarized tunneling into superconductors [14] has been first used to demonstrate spin-filter tunneling in FM Eu chalcogenides, such as EuS [15], EuSe [16], and EuO [17]. More recently, SF-MTJs have been utilized to explore a spin-filter TMR effect controlled by the relative magnetization orientation of an FM barrier layer and an FM counter electrode. Complex FM (or ferrimagnetic) oxide materials such as CoFe_2O_4 [18, 19], NiFe_2O_4 [20], NiMn_2O_4

[21,22], CoCr_2O_4 and MnCr_2O_4 [23] have been used in these experiments. Very recently 2D van der Waals materials, such as CrI_3 [24-26], CrBr_3 [27], and CrSe_3 [28], have been explored as FM barriers in SF-MTJs and demonstrated large spin-filter TMR effects.

In recent years, the emphasis of spintronics has been shifted from ferromagnets to antiferromagnets due to their advantages such as robustness against magnetic perturbations, absence of stray fields, and ultrafast spin dynamics [29-33]. Especially interesting appeared to be antiferromagnetic (AFM) crystals breaking PT and $U\tau_{1/2}$ symmetries (where P is space inversion, T is time reversal, U is spin-flip, and $\tau_{1/2}$ is half a unit cell translation) and thus producing momentum-dependent spin polarization, even in the absence of spin-orbit coupling (SOC) [34-43]. This subgroup of collinear antiferromagnets is now known as “altermagnets” [41,42]. Due to their spin-polarized band structure, altermagnets are predicted to exhibit spin-dependent transport properties [44]. Particularly interesting are AFM tunnel junctions (AFMTJs) with altermagnetic (AM) metals electrodes, whose relative Néel vector orientation controls the TMR effect [45-50].

While there has been an extensive endeavor to utilize AM metals in spintronic devices such as AFMTJs, AM insulators (AMIs) remained largely unexplored in the realm of AFM spintronics. It is notable, however, that among the predicted altermagnets, the majority (around 80%) are insulators [51]. It is therefore interesting to explore their spin-dependent properties in view of potential spintronic applications. One of the emerging questions, in this regard, is if AMIs could be used as efficient spin-filter barrier materials in SF-MTJs to generate highly spin-polarized currents and produce strong spin-filter TMR effects.

In this letter, we address this question by analyzing the complex band structure of rutile-type AMIs MF_2 ($M = \text{Fe, Co, Ni}$). We demonstrate that evanescent states in these AMIs exhibit

spin- and momentum-dependent decay rates resulting in a large momentum-dependent spin polarization of the electric current tunneling across them. Based on these results, we estimate the TMR effect in SF-MTJs that consist of two MF_2 (001) barriers whose Néel vector can be switched to be parallel or antiparallel. We predict a sizable spin-filter TMR effect of about 150-170% in SF-MTJs based on AMI CoF_2 and NiF_2 . Our results show that AMIs can be efficiently employed in spintronics as a viable alternative to conventional FM spin-filter materials.

Owing to the nonrelativistic spin splitting of AMIs, these materials exhibit evanescent states with different decay rates $\kappa^{\uparrow,\downarrow}(\vec{k}_{\parallel})$ for up- (\uparrow) and down- (\downarrow) spin electrons. Their decay rates depend on the wave vector $\vec{k}_{\parallel} = (k_x, k_y)$ that is transverse to the transport direction and conserved in the tunneling process. Due to the exponential dependence of the transmission probability $\sim e^{-2\kappa^{\uparrow,\downarrow}(\vec{k}_{\parallel})d}$, where d is the barrier thickness, the transmitted electrons are spin polarized. We define the \vec{k}_{\parallel} -dependent spin-filtering factor of the AMI barrier as $f(\vec{k}_{\parallel}) = \kappa^{\downarrow}(\vec{k}_{\parallel}) - \kappa^{\uparrow}(\vec{k}_{\parallel})$, which implies that up- (down-) spin electrons are transmitted more efficiently across the barrier for positive (negative) f . For a normal insulator, the spin-filtering factor $f(\vec{k}_{\parallel}) = 0$ [Fig. 1(b)], while for an AMI, $f(\vec{k}_{\parallel}) \neq 0$ [Fig. 1(c)]. If a non-spin polarized current from a normal metal (NM) [Fig. 1(a)] is transmitted across such AMI, it acquires \vec{k}_{\parallel} -dependent spin polarization $p(\vec{k}_{\parallel}) = \frac{e^{-2\kappa^{\downarrow}(\vec{k}_{\parallel})d} - e^{-2\kappa^{\uparrow}(\vec{k}_{\parallel})d}}{e^{-2\kappa^{\downarrow}(\vec{k}_{\parallel})d} + e^{-2\kappa^{\uparrow}(\vec{k}_{\parallel})d}} = \tanh[f(\vec{k}_{\parallel})d]$, as illustrated in Fig. 1(d). In AMIs which host mirror symmetries, M_x and M_y , such as MnF_2 (001) [52] and CoF_2 (001) [53], the spin-filtering factor obeys $M_x f(k_x, k_y) = -f(-k_x, k_y)$ and $M_y f(k_x, k_y) = -f(k_x, -k_y)$. As a result, $f(\vec{k}_{\parallel})$ and $p(\vec{k}_{\parallel})$ exhibit a d -wave shape with alternating sign in every quadrant of the (001) two-dimensional Brillouin zone (2DBZ) [Figs. 1(c,d)].

The \vec{k}_{\parallel} -dependent spin polarization of AFIs can be used to achieve spin-filter TMR in SF-MTJs representing two NM electrodes separated by a composite barrier layer [Figs. 1(e,f)]. The latter consists of two AMIs separated by a normal insulator to magnetically decouple the two AMIs. When the Néel vector is parallel [Fig. 1(e)], the spin-filtering factors $f(\vec{k}_{\parallel})$ of the AMIs match at each \vec{k}_{\parallel} . This allows electrons with a given spin (either up or down) to be efficiently transmitted across both AMI layers in those regions of the 2DBZ where $|f(\vec{k}_{\parallel})|$ is large, thus supporting a large tunneling current. On the contrary, when the Néel vector is antiparallel [Fig. 1(f)], the spin-filtering factors $f(\vec{k}_{\parallel})$ of the AMIs mismatch. In this case, those electrons which have been efficiently transmitted across the first AMI layer are filtered out in the second AMI layer due to the spin mismatch, thus suppressing the tunneling current. As a result, the transmission probability $T_P(\vec{k}_{\parallel})$ for the parallel-aligned SF-MTJ [Fig. 1(e)] is larger than the transmission probability $T_{AP}(\vec{k}_{\parallel})$ for

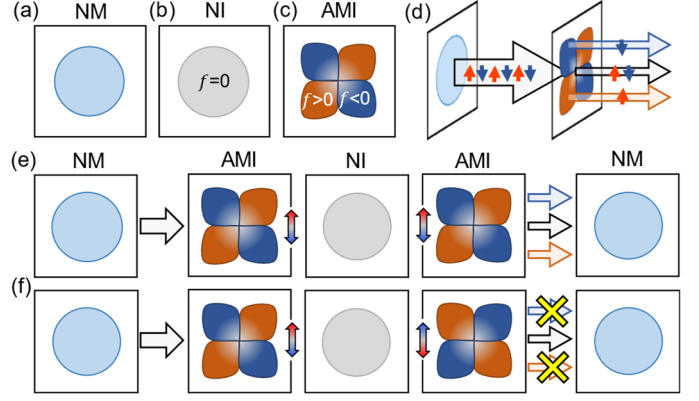


Fig. 1 (a-c) Schematic views of normal metal (NM) with spin-independent Fermi surface (a), normal insulator (NI) with zero spin filtering factor (b), and altermagnetic insulator (AMI) with a non-zero \vec{k}_{\parallel} -dependent spin-filtering factor. (d) Schematic mechanism for the \vec{k}_{\parallel} -dependent tunneling spin polarization in a tunnel junction with a NM electrode and an AMI barrier. Block arrows indicate electric current. Red and blue arrows indicate up and down spins. (e,f) Schematic of SF-MTJ with a composite barrier which consists of two AMI layers separated by an NI layer for parallel (e) and antiparallel (f) Néel vector. Double arrows indicate the Néel vector in AMIs.

the antiparallel-aligned SF-MTJ [Fig. 1(f)]. This leads to a \vec{k}_{\parallel} -dependent spin-filter $TMR(\vec{k}_{\parallel}) = \frac{T_P(\vec{k}_{\parallel}) - T_{AP}(\vec{k}_{\parallel})}{T_{AP}(\vec{k}_{\parallel})}$ and a finite net spin-filter $TMR = \frac{T_P - T_{AP}}{T_{AP}}$, where $T_P = \frac{1}{N_k} \sum_{\vec{k}_{\parallel}} T_P(\vec{k}_{\parallel})$, $T_{AP} = \frac{1}{N_k} \sum_{\vec{k}_{\parallel}} T_{AP}(\vec{k}_{\parallel})$, and N_k is the number of k -points.

To achieve an efficient spin-filtering effect, AMIs with a large spin splitting are required to support spin-dependent decay rates $\kappa^{\uparrow,\downarrow}$. Among AMIs, fluoride compounds are reported to have a sizable spin splitting [51]. Therefore, to demonstrate the spin-filtering effect, as representative AMIs, we consider rutile fluorides MF_2 ($M = Mn, Co, Ni$) whose atomic structure is shown in Fig. 2(a) (space group $P4_2/mnm$ [54]). The magnetic moment of the metal atom $M1$ at the center of the unit cell is opposite to that of the $M2$ atoms at the corners. The Néel vector is pointing along the [001] direction in MnF_2 [52] and CoF_2 [53], and along the [010] direction in NiF_2 [55].

We perform density-functional theory (DFT) calculations of the electronic and magnetic structure of bulk MF_2 crystals, as described in Supplementary Material [56]. These calculations predict that MnF_2 , CoF_2 , and NiF_2 have indirect band gaps of 4.14, 4.36 and 4.30 eV, respectively. The magnetic moments at the Mn, Co, Ni sites are found to be 4.95, 2.90, and 1.78 μ_B , indicating a nominal 2+ valence of the M ions with high-spin states exhibiting $d^5 [t_{2g}(3\uparrow), e_g(2\uparrow)]$, $d^6 [t_{2g}(3\uparrow, 2\downarrow), e_g(2\uparrow)]$, and $d^8 [t_{2g}(3\uparrow, 3\downarrow), e_g(2\uparrow)]$ occupancies, respectively. The calculated band gaps of the MF_2 compounds and their magnetic moments are in good agreement with the experimental observations [52,53,55] and the earlier calculations [36,51].

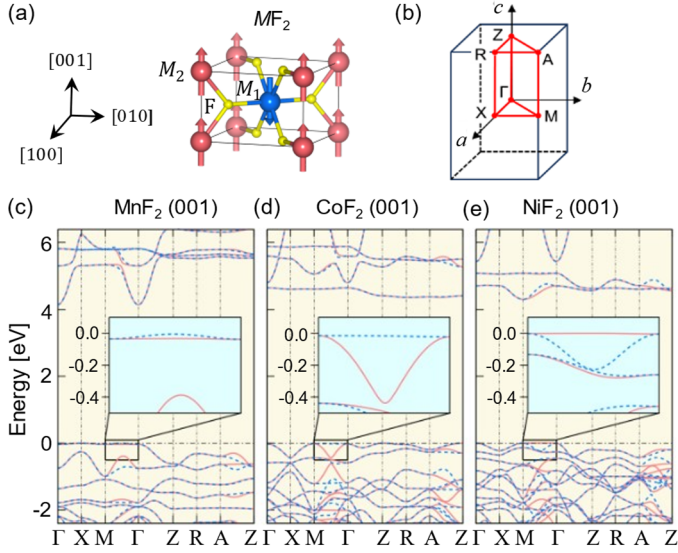


Fig. 2 (a) Atomic and magnetic structure of AMI MF_2 . (b) Tetragonal Brillouin zone of MF_2 with high-symmetry points and lines indicated. (c-e) Band structure of MnF_2 (c), CoF_2 (d), and NiF_2 (e) calculated without spin-orbit coupling. Red and blue curves indicate up- and down-spin bands, respectively. Zero energy is set to the VBM. Insets show the band structure in the vicinity of the VBM (-0.5 eV to 0.1 eV) along the Γ -M direction.

The magnetic space group of the MF_2 crystals has broken PT or $U\tau_{1/2}$ symmetries and exhibits glide $G_x = \{M_x | (\frac{1}{2}, \frac{1}{2}, \frac{1}{2})\}$, $G_y = \{M_y | (\frac{1}{2}, \frac{1}{2}, \frac{1}{2})\}$ and mirror M_z symmetries. In the absence of SOC, these symmetries enforce spin-degenerate bands at the k -planes invariant to G_x and G_y , such as $k_x = 0, \pi/2$ and $k_y = 0, \pi/2$, whereas spin splitting is not constrained away from these planes. This is evident from Figs. 2(c-e), showing that the electronic bands of MF_2 are spin degenerate along the Γ -X, Γ -Z, Γ -Z, X-M, Z-R, and R-A directions lying in these glide-invariant planes, while they are spin-split along the Γ -M and Z-A directions, going away from these planes. We find a large spin splitting of about 0.44 eV in the vicinity of the VBM for CoF_2 [inset of Fig. 2(d)], whereas it is about 0.03 eV and 0.21 eV for MnF_2 and NiF_2 , respectively [insets of Figs. 2(c,e)]. For all the MF_2 compounds, spin splitting around the conduction band minimum (CBM) is notably smaller than that near the VBM.

Due to this spin splitting, the \vec{k}_{\parallel} -dependent potential barrier for tunneling up- and down-spin electrons is different. This leads to spin-dependent evanescent states with different decay rates $\kappa^{\uparrow,\downarrow}$ for electrons with opposite spin. The evanescent states in insulators are determined by the complex band structure in the energy-gap region [10-13]. To obtain the complex band structure, we calculate the wave vector k_z parallel to the transport direction as a function of \vec{k}_{\parallel} and energy E using the dispersion relation $E = E(\vec{k}_{\parallel}, k_z^{\uparrow,\downarrow})$ allowing complex solutions for $k_z^{\uparrow,\downarrow} = q^{\uparrow,\downarrow} + i\kappa^{\uparrow,\downarrow}$. The imaginary part $\kappa^{\uparrow,\downarrow}$ is the spin-dependent decay rate that

determines the wave function $\sim e^{-\kappa^{\uparrow,\downarrow}d}$. The evanescent states with the lowest decay rate are expected to be most efficient in the tunneling process and hence control transmission.

Figs. 3(a-c) show the calculated complex band structure of CoF_2 (001) at different \vec{k}_{\parallel} -points [for MnF_2 and NiF_2 , see Figs. S1(a-c) and S2(a-c)]. These complex bands are connected to the real bands with the same curvature at the connecting points due to the analytic properties of the $E(\vec{k}_{\parallel}, k_z^{\uparrow,\downarrow})$ function [Figs. S3-S5]. The complex bands at energies in the band gap of MF_2 (001) determine the evanescent states of interest. It is seen that at $\vec{k}_{\parallel} = (0, 0)$, i.e. at the $\bar{\Gamma}$ point, the complex bands are spin degenerate [Figs. 3(a), S1(a), and S2(a)], due to the spin degeneracy of the real bands along the Γ -Z line by symmetry [Figs. 2(c-e)]. Away from the $\bar{\Gamma}$ point (and \bar{M} points) in the 2DBZ, the complex bands are spin-split, as seen from Figs. 3(b,c) for CoF_2 and Figs. S1(b,c) and S2(b,c) for MnF_2 and NiF_2 , reflecting the spin splitting of the real bands away from the $G_{x,y}$ invariant planes [Figs. 2(c-e)]. For example, in CoF_2 (001), at $E = E_{VBM} + 0.1$ eV and $\vec{k}_{\parallel} = (0.3, 0.3)$, the lowest decay rates are $\kappa^{\uparrow} = 0.36 \text{ \AA}^{-1}$ and $\kappa^{\downarrow} = 0.23 \text{ \AA}^{-1}$ [indicated by blue and red circles in Fig. 3(b)].

Figs. 3(d-f) show the calculated distribution of the lowest decay rates $\kappa^{\uparrow,\downarrow}(\vec{k}_{\parallel})$ in the 2DBZ for different energies within the band gap of CoF_2 (001) [for MnF_2 (001) and NiF_2 (001), see Figs. S1(d-f) and S2(d-f)]. We observe a sizable spin dependence of $\kappa^{\uparrow,\downarrow}(\vec{k}_{\parallel})$, especially along the $\bar{\Gamma}$ - \bar{M} direction for energies close to the VBM, e.g. $E = E_{VBM} + 0.1$ eV [Fig. 3(d)]. This reflects a sizable $f(\vec{k}_{\parallel})$ in CoF_2 [Fig. S6(d)], exceeding that in MnF_2 and NiF_2 [Figs. S6(a,g)]. For energies close to the middle of the gap (MG), $E = E_{MG}$, the decay rates become nearly spin independent [Figs. 3(e), S1(e) and S2(e)]. This reflects nearly vanishing $f(\vec{k}_{\parallel})$ [Figs. S6(b,e,h)] due to the nearly spin degenerate complex bands at the midgap energy E_{MG} of MF_2 (001) [Figs. 3(b), S1(b), and S2(b)]. For energies close to the CBM, spin dependence of $\kappa^{\uparrow,\downarrow}(\vec{k}_{\parallel})$ and $f(\vec{k}_{\parallel})$ is less pronounced than that for the energies close to the VBM for all three compounds CoF_2 , MnF_2 , and NiF_2 [Figs. 3(f), S1(f), S2(f), and S6(c-i)]. For example, at $E = E_{CBM} - 0.1$ eV, the lowest decay rates in CoF_2 (001) are $\kappa^{\uparrow} = 0.37 \text{ \AA}^{-1}$ and $\kappa^{\downarrow} = 0.41 \text{ \AA}^{-1}$ [indicated by blue and red circles in Fig. 3(c)].

The spin-dependent decay rates $\kappa^{\uparrow,\downarrow}(\vec{k}_{\parallel})$ and non-zero spin-filtering factors $f(\vec{k}_{\parallel})$ in AMIs MF_2 lead to \vec{k}_{\parallel} -dependent spin polarization $p(\vec{k}_{\parallel}) = \tanh[f(\vec{k}_{\parallel})d]$. For example, at $E = E_{VBM} + 0.1$ eV and barrier thickness $d = 2$ nm, $|p(\vec{k}_{\parallel})|$ is sizable in a wide region of the 2DBZ [Figs. 4(a-c)]. Especially large $|p(\vec{k}_{\parallel})|$ is in CoF_2 and NiF_2 approaching 100% at certain \vec{k}_{\parallel} for energies close to the VBM. We also observe a sizable $|p(\vec{k}_{\parallel})|$ at $E = E_{CBM} - 0.1$ eV, though in much narrower regions of the 2DBZ [Fig. S7].

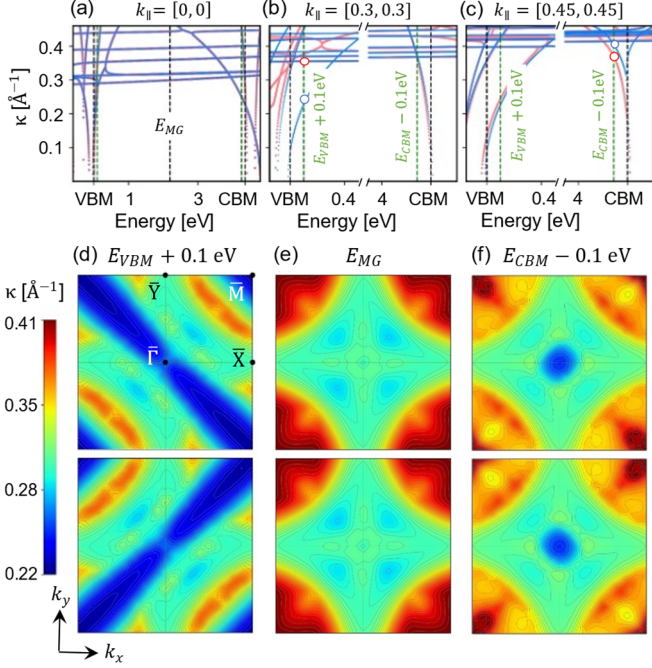


Fig. 3 (a-c) Complex band structures of CoF₂ (001) as a function of energy at three different $\vec{k}_{\parallel} = (k_x, k_y)$ along the $\bar{\Gamma} - \bar{M}$ line. (d-f) Distribution of lowest decay rates for up-spin (upper panels) and down-spin (lower panels) evanescent states in the band gap of CoF₂ (001) as a function of $\vec{k}_{\parallel} = (k_x, k_y)$ in the 2DBZ at (d) $E = E_{VBM} + 0.1$ eV, (e) $E = E_{MG}$, and (f) $E = E_{CBM} - 0.1$ eV.

The predicted \vec{k}_{\parallel} -dependent spin polarization $p(\vec{k}_{\parallel})$ can be functionalized in SF-MTJs to produce spin-filter TMR [Figs. 1(e,f)]. To estimate the TMR ratio, we employ a model of spin-filter tunneling through a double potential barrier whose spin-dependent energy profile depends on the relative Néel vector orientation of the two AMI layers. For simplicity, we assume \vec{k}_{\parallel} -independent conduction channels in the NM electrodes and ignore contribution from the non-magnetic spacer layer separating AMIs. Assuming equal thickness d of the two AMI layers, we estimate tunneling transmission for parallel- [$T_P(\vec{k}_{\parallel})$] and antiparallel- [$T_{AP}(\vec{k}_{\parallel})$] aligned SF-MTJ, as follows:

$$T_P(\vec{k}_{\parallel}) \propto \left[e^{-2\kappa^{\uparrow}(\vec{k}_{\parallel})d} e^{-2\kappa^{\downarrow}(\vec{k}_{\parallel})d} + e^{-2\kappa^{\downarrow}(\vec{k}_{\parallel})d} e^{-2\kappa^{\uparrow}(\vec{k}_{\parallel})d} \right], \quad (1)$$

$$T_{AP}(\vec{k}_{\parallel}) \propto \left[e^{-2\kappa^{\uparrow}(\vec{k}_{\parallel})d} e^{-2\kappa^{\uparrow}(\vec{k}_{\parallel})d} + e^{-2\kappa^{\downarrow}(\vec{k}_{\parallel})d} e^{-2\kappa^{\downarrow}(\vec{k}_{\parallel})d} \right], \quad (2)$$

where $\kappa^{\uparrow,\downarrow}(\vec{k}_{\parallel})$ are lowest decay rates obtained from the complex band structure. Figs. 4(d-f) and 4(g-i) show the calculated $T_P(\vec{k}_{\parallel})$ and $T_{AP}(\vec{k}_{\parallel})$ for $E = E_{VBM} + 0.1$ eV and $d = 2$ nm. It is seen that $T_P(\vec{k}_{\parallel})$ exhibits a pattern resembling an overlap of the distribution patterns of $\kappa^{\uparrow}(\vec{k}_{\parallel})$ and $\kappa^{\downarrow}(\vec{k}_{\parallel})$ [e.g., compare Figs. 4(e) and 3(d)]. While $T_{AP}(\vec{k}_{\parallel})$ also exhibits a qualitatively

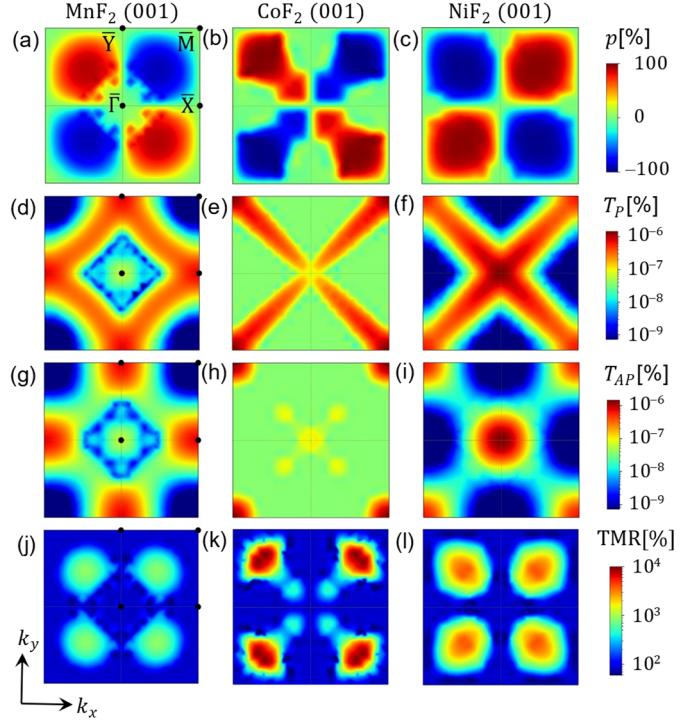


Fig. 4 Transport properties of MnF₂ (a,d,g,j), CoF₂ (b,e,h,k) and NiF₂ (c,f,i,l) AMIs at $E = E_{VBM} + 0.1$ eV. (a-c) \vec{k}_{\parallel} -dependent spin polarization $p(\vec{k}_{\parallel}) = \tanh[f(\vec{k}_{\parallel})d]$. (d-i) \vec{k}_{\parallel} -dependent transmission across an SF-MTJ for parallel (d-f) and antiparallel (g-i) Néel vectors. (j-l) \vec{k}_{\parallel} -resolved $TMR(\vec{k}_{\parallel}) = \frac{T_P(\vec{k}_{\parallel}) - T_{AP}(\vec{k}_{\parallel})}{T_{AP}(\vec{k}_{\parallel})}$. In (e) and (h), $T_P(\vec{k}_{\parallel})$ and $T_{AP}(\vec{k}_{\parallel})$ are scaled by a factor of 50 for a better view.

similar pattern, it features greatly suppressed transmission in the 2DBZ regions with the strongest contrast between $\kappa^{\uparrow}(\vec{k}_{\parallel})$ and $\kappa^{\downarrow}(\vec{k}_{\parallel})$ [e.g., around the middle of the $\bar{\Gamma} - \bar{M}$ lines in Figs. 4(g,i)]. Figs. 4(j-l) show the calculated \vec{k}_{\parallel} -resolved TMR ratio, $TMR(\vec{k}_{\parallel}) = \frac{T_P(\vec{k}_{\parallel}) - T_{AP}(\vec{k}_{\parallel})}{T_{AP}(\vec{k}_{\parallel})}$, at $E = E_{VBM} + 0.1$ eV. Giant contributions to TMR close to 10⁴% are seen from those regions in the 2DBZ where the spin polarization is approaching 100% [Figs. 4(a-c)]. This reflects the fact that $TMR(\vec{k}_{\parallel})$ and $p(\vec{k}_{\parallel})$ are related by Julliere's formula [3], $TMR(\vec{k}_{\parallel}) = \frac{2p^2(\vec{k}_{\parallel})}{1-p^2(\vec{k}_{\parallel})}$. Fig. 5 shows the total TMR ratio as a function of the Fermi energy. For all three compounds, we observe a strong enhancement of spin-filtering TMR at energies close to VBM with values of about 150–170 % for CoF₂ and NiF₂.

Our results demonstrate that AMIs MF_2 can be used as spin-filter materials in SF-MTJs provided that the Fermi energy can be tuned close to the VBM of the AMI. This can be achieved, e.g., by utilizing polar interfaces which allow varying the band offset between metals and insulators in a broad range of energies (see, e.g., Refs. [57,58]). To magnetically decouple two AMIs,

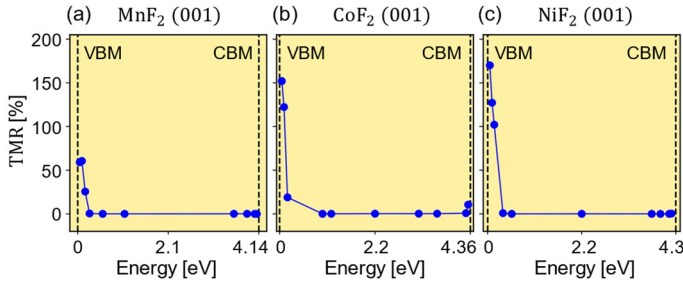


Fig. 5 Spin-filter $TMR = \frac{T_P - T_{AP}}{T_{AP}}$ as a function of the Fermi energy for SF-MTJs based on MnF_2 (001) (a), CoF_2 (001) (b), and NiF_2 (001) (c).

one can use a non-magnetic insulator ZnF_2 which has the rutile structure and a very similar lattice constant [54].

We note that due to the mirror symmetries, \hat{M}_x and \hat{M}_y , the net tunneling spin polarization $p = \sum_{\vec{k}_{\parallel}} p(\vec{k}_{\parallel})$ of MF_2 (001) is zero for transport along the [001] direction. To obtain a finite net spin polarization, layer stacking with a low-symmetry surface is needed to break these symmetries. This can be achieved for transport along the [110] direction. Indeed, our calculations find a large net spin polarization for MnF_2 (110) at $E = E_{VBM} + 0.1$ eV [Figs. S8 and S9]. This property allows using AMIs as FM insulators in SF-MTJs.

Overall, our results indicate that AMIs can be efficiently employed in AFM spintronics to achieve strong spin-filtering

effects. Using rutile fluorides MF_2 ($M = Mn, Co, Ni$), as representative examples, we have predicted that these AMIs exhibit a large \vec{k}_{\parallel} -dependent spin polarization when the Fermi energy is tuned close to the VBM. This property allows realizing sizable spin-filter TMR in SF-MTJs based on these AMIs. Apart from rutile fluorides, there are numerous AMIs which may exhibit similar spin-filtering properties. We therefore hope that our results will motivate experimentalists working in this field to verify our predictions.

Acknowledgments. This work was supported by the National Science Foundation (Grant No. DMR-2316665) and UNL’s Grand Challenges catalyst award “Quantum Approaches Addressing Global Threats.” D.-F.S. acknowledges support from the National Key R&D Program of China (Grant No. 2021YFA1600200), the National Natural Science Foundation of China (Grants Nos. 12274411, 12241405, and 52250418), the Basic Research Program of the Chinese Academy of Sciences Based on Major Scientific Infrastructures (Grant No. JZHKYPT-2021-08), and the CAS Project for Young Scientists in Basic Research (Grant No. YSBR-084). Computations were performed at the University of Nebraska Holland Computing Center.

*ksamanta2@unl.edu

†dfshao@issp.ac.cn

‡tsymbal@unl.edu

1. E. Y. Tsymlal and I. Žutić, Eds., *Spintronics Handbook: Spin Transport and Magnetism*, 2-nd edition (CRC press, 2019).
2. T. S. Santos and J. S. Moodera, Spin Filter Tunneling, in *Spintronics Handbook: Spin Transport and Magnetism*, Eds. E. Y. Tsymlal and I. Zutic (CRC press, 2019).
3. M. Jullière, Tunneling between ferromagnetic films, *Phys. Lett. A* **54**, 225 (1975).
4. S. Maekawa and U. Gafvert, Electron-tunneling between ferromagnetic films, *IEEE Trans. Magn.* **MAG-18**, 707 (1982).
5. J. S. Moodera, L. R. Kinder, T. M. Wong, and R. Meservey, Large magnetoresistance at room temperature in ferromagnetic thin film tunnel junctions, *Phys. Rev. Lett.* **74**, 3273 (1995).
6. S. Yuasa, T. Nagahama, A. Fukushima, Y. Suzuki, and K. Ando, Giant room-temperature magnetoresistance in single-crystal Fe/MgO/Fe magnetic tunnel junctions, *Nat. Mater.* **3**, 868 (2004).
7. S. S. P. Parkin, C. Kaiser, A. Panchula, P. M. Rice, B. Hughes, M. Samant, and S. H. Yang, Giant tunneling magnetoresistance at room temperature with MgO (100) tunnel barriers, *Nat. Mater.* **3**, 862 (2004).
8. E. Y. Tsymlal, O. N. Mryasov, and P. R. LeClair, Spin-dependent tunneling in magnetic tunnel junctions, *J. Phys.: Cond. Matt.* **15**, R109 (2003).
9. V. Heine, On the general theory of surface states and scattering of electrons in solids. *Proc. Phys. Soc.* **81**, 300 (1963); Theory of surface states. *Phys. Rev.* **138**, A1689 (1965).
10. P. Mavropoulos, N. Papanikolaou, and P. Dederichs, Complex band structure and tunneling through ferromagnet/insulator/ferromagnet junctions, *Phys. Rev. Lett.* **85**, 1088 (2000).
11. W. H. Butler, X.-G. Zhang, T. C. Schulthess, and J. M. MacLaren, Spin-dependent tunneling conductance of Fe/MgO/Fe sandwiches, *Phys. Rev. B* **63**, 054416 (2001).
12. J. P. Velev, K. D. Belashchenko, D. Stewart, M. van Schilfgaarde, S. S. Jaswal, and E. Y. Tsymlal, Negative spin-polarization and large tunneling magnetoresistance in epitaxial Co/SrTiO₃/Co magnetic tunnel junctions, *Phys. Rev. Lett.* **95**, 216601 (2005).
13. P. V. Lukashev, et al. Spin filtering with EuO: Insight from the complex band structure, *Phys. Rev. B* **85**, 224414 (2012).
14. R. Meservey and P. M. Tedrow, Spin-polarized electron tunneling, *Phys. Rep.* **238**, 173 (1994).
15. J. S. Moodera, X. Hao, G. A. Gibson, and R. Meservey, Electron-spin polarization in tunnel junctions in zero applied field with ferromagnetic EuS barriers, *Phys. Rev. Lett.* **61**, 637 (1988).
16. J. S. Moodera, R. Meservey, and X. Hao, Variation of the electron-spin polarization in EuSe tunnel junctions from zero to near 100% in a magnetic field, *Phys. Rev. Lett.* **70**, 853 (1993).
17. T. S. Santos and J. S. Moodera, Observation of spin filtering with a ferromagnetic EuO tunnel barrier, *Phys. Rev. B* **69**, 241203 (2004).
18. M. G. Chapline and S. X. Wang. Room-temperature spin filtering in a $CoFe_2O_4/MgAl_2O_4/Fe_3O_4$ magnetic tunnel barrier, *Phys. Rev. B* **74**, 014418 (2006).

19. A. V. Ramos, M.-J. Guittet, J.-B. Moussy, R. Mattana, C. Deranlot, F. Petroff, C. Gatel, Room temperature spin filtering in epitaxial cobalt-ferrite tunnel barriers, *Appl. Phys. Lett.* **91**, 122107 (2007).
20. S. Matzen, J.-B. Moussy, P. Wei, C. Gatel, J. C. Cezar, M. A. Arrio, Ph. Sainctavit, and J. S. Moodera, Structure, magnetic ordering, and spin filtering efficiency of NiFe₂O₄(111) ultrathin films, *Appl. Phys. Lett.* **104**, 182404 (2014).
21. U. Lüders, M. Bibes, K. Bouzehouane, E. Jacquet, J.-P. Contour, S. Fusil, J.-F. Bobo, J. Fontcuberta, A. Barthélémy, and A. Fert, Spin filtering through ferrimagnetic NiFe₂O₄ tunnel barriers, *Appl. Phys. Lett.* **88**, 082505 (2006).
22. B. B. Nelson-Cheeseman, R.V. Chopdekar, L. M. B. Allredge, J. S. Bettinger, E. Arenholz, and Y. Suzuki, Probing the role of the barrier layer in magnetic tunnel junction transport, *Phys. Rev. B* **76**, 220410(R) (2007).
23. R. V. Chopdekar, B. B. Nelson-Cheeseman, M. Liberati, E. Arenholz, and Y. Suzuki, Role of magnetic anisotropy in spin-filter junctions, *Phys. Rev. B* **83**, 224426 (2011).
24. T. Song, X. Cai, M. W.-Y. Tu, X. Zhang, B. Huang, N. P. Wilson, K. L. Seyler, L. Zhu, T. Taniguchi, K. Watanabe, M. A. McGuire, D. H. Cobden, D. Xiao, W. Yao, and X. Xu, Giant tunneling magnetoresistance in spin-filter van der Waals heterostructures, *Science* **360**, 1214 (2018).
25. T. Song, M. W.-Y. Tu, C. Carnahan, X. Cai, T. Taniguchi, K. Watanabe, M. A. McGuire, D. H. Cobden, D. Xiao, W. Yao, and X. Xu, Voltage control of a van der Waals spin-filter magnetic tunnel junction, *Nano Lett.* **19**, 915 (2019).
26. T. R. Paudel and E. Y. Tsymbal, Spin filtering in CrI₃ tunnel junctions, *ACS Appl. Mater. Interfaces* **11**, 15781 (2019).
27. L. Pan, L. Huang, M. Zhong, X.-W. Jiang, H.-X. Deng, J. Li, J.-B. Xiaa, and Z. Wei, Large tunneling magnetoresistance in magnetic tunneling junctions based on two-dimensional CrX₃ (X = Br, I) monolayers, *Nanoscale* **10**, 22196 (2018).
28. J. Feng, K. Li, M. Zheng, W. Zhang, Y. Liu, D. Wang, Z. Zhang, C. Zuo, R. Xiong, and Z. Lu, Excellent spin-filtering and giant tunneling magnetoresistance in a dual-electrode van der Waals magnetic tunnel junction based on ferromagnetic CrSe₂, *Appl. Surf. Sci.* **611**, 155588 (2023).
29. T. Jungwirth, X. Marti, P. Wadley, and J. Wunderlich, J. Antiferromagnetic spintronics. *Nat. Nanotech.* **11**, 231 (2016).
30. V. Baltz, A. Manchon, M. Tsoi, T. Moriyama, T. Ono, and Y. Tserkovnyak, Antiferromagnetic spintronics, *Rev. Mod. Phys.* **90**, 015005 (2018).
31. T. Jungwirth, J. Sinova, A. Manchon, X. Marti, J. Wunderlich, and C. Felser, The multiple directions of antiferromagnetic spintronics, *Nat. Phys.* **14**, 200 (2018).
32. J. Železný, P. Wadley, K. Olejník, A. Hoffmann, and H. Ohno, Spin transport and spin torque in antiferromagnetic devices. *Nat. Phys.* **14**, 220 (2018).
33. L. Šmejkal, Y. Mokrousov, B. Yan, and A. H. MacDonald, Topological antiferromagnetic spintronics. *Nat. Phys.* **14**, 242 (2018).
34. S. Hayami, Y. Yanagi, and H. Kusunose, Momentum-dependent spin splitting by collinear antiferromagnetic ordering, *J. Phys. Soc. Jpn.* **88**, 123702 (2019).
35. M. Naka, S. Hayami, H. Kusunose, Y. Yanagi, Y. Motome, and H. Seo, Spin current generation in organic antiferromagnets, *Nat. Commun.* **10**, 4305 (2019).
36. L.-D. Yuan, Z. Wang, J.-W. Luo, E. I. Rashba, and A. Zunger, Giant momentum-dependent spin splitting in centrosymmetric low-Z antiferromagnets, *Phys. Rev. B* **102**, 014422 (2020).
37. S. Hayami, Y. Yanagi, and H. Kusunose, Bottom-up design of spin-split and reshaped electronic band structures in antiferromagnets without spin-orbit coupling: Procedure on the basis of augmented multipoles, *Phys. Rev. B* **102**, 144441 (2020).
38. L.-D. Yuan, Z. Wang, J.-W. Luo, and A. Zunger, A. Prediction of low-Z collinear and noncollinear antiferromagnetic compounds having momentum-dependent spin splitting even without spin-orbit coupling, *Phys. Rev. Mater.* **5**, 014409 (2021).
39. H. Y. Ma, M. Hu, N. Li, J. Liu, W. Yao, J.-F. Jia, and J. Liu, Multifunctional antiferromagnetic materials with giant piezomagnetism and noncollinear spin current, *Nat. Commun.* **12**, 2846 (2021).
40. P. Liu, J. Li, J. Han, X. Wan, and Q. Liu, Spin-group symmetry in magnetic materials with negligible spin-orbit coupling, *Phys. Rev. X* **12**, 021016 (2022).
41. L. Šmejkal, J. Sinova, and T. Jungwirth, Beyond conventional ferromagnetism and antiferromagnetism: A phase with nonrelativistic spin and crystal rotation symmetry, *Phys. Rev. X* **12**, 031042 (2022).
42. L. Šmejkal, J. Sinova, and T. Jungwirth, Emerging research landscape of altermagnetism, *Phys. Rev. X* **12**, 040501 (2022).
43. L. Yuan and A. Zunger, Degeneracy removal of spin bands in collinear antiferromagnets with non-interconvertible spin-structure motif pair, *Adv. Mater.* **35**, 2211966 (2023).
44. R. González-Hernández, L. Šmejkal, K. Výborný, Y. Yahagi, J. Sinova, T. Jungwirth, and J. Železný, Efficient electrical spin-splitter based on non-relativistic collinear antiferromagnetism, *Phys. Rev. Lett.* **126**, 127701 (2021).
45. D.-F. Shao, S. H. Zhang, M. Li, C. B. Eom, and E. Y. Tsymbal, Spin-neutral currents for spintronics, *Nat. Commun.* **12**, 7061 (2021).
46. L. Šmejkal, A. Birk Hellenes, R. González-Hernández, J. Sinova, and T. Jungwirth, Giant and tunneling magnetoresistance in unconventional collinear antiferromagnets with nonrelativistic spin-momentum coupling, *Phys. Rev. X* **12**, 011028 (2022).
47. D. F. Shao, Y. Y. Jiang, J. Ding, S. H. Zhang, Z. A. Wang, R. C. Xiao, G. Gurung, W. J. Lu, Y. P. Sun, and E. Y. Tsymbal, Néel spin currents in antiferromagnets, *Phys. Rev. Lett.* **130**, 216702 (2023).
48. Y.-Y. Jiang, Z.-A. Wang, K. Samanta, S.-H. Zhang, R.-C. Xiao, W. J. Lu, Y. P. Sun, E. Y. Tsymbal, and D.-F. Shao, Prediction of giant tunneling magnetoresistance in RuO₂/TiO₂/RuO₂ (110) antiferromagnetic tunnel junctions, *Phys. Rev. B* **108**, 174439 (2023).
49. B. Chi, L. Jiang, Y. Zhu, G. Yu, C. Wan, J. Zhang, and X. Han, Crystal-facet-oriented altermagnets for detecting ferromagnetic and antiferromagnetic states by giant tunneling magnetoresistance, *Phys. Rev. Applied* **21**, 034038 (2024).
50. K. Samanta, Y.-Y. Jiang, T. R. Paudel, D.-F. Shao, and E. Y. Tsymbal, Tunneling magnetoresistance in magnetic tunnel junctions with a single ferromagnetic electrode, *Phys. Rev. B* **109**, 174407 (2024).
51. Y. Guo, H. Liu, O. Janson, I. C. Fulga, J. van den Brink, and J. I. Facio, Spin-split collinear antiferromagnets: A large-scale ab-initio study, *Mater. Today Phys.* **32**, 100991(2023).

52. Z. Yamani, Z. Tun, and D. H. Ryan, Neutron scattering study of the classical antiferromagnet MnF_2 : a perfect hands-on neutron scattering teaching course, *Can. J. Phys.* **88**, 771 (2010).
53. W. Jauch, M. Reehuis, and A. J. Schultz, γ -ray and neutron diffraction studies of CoF_2 : magnetostriction, electron density and magnetic moment, *Acta Crystallogr. A* **60**, 51 (2003).
54. J. W. Stout and S. A. Reed, The crystal structure of MnF_2 , FeF_2 , CoF_2 , NiF_2 and ZnF_2 , *J. Am. Chem. Soc.* **76**, 5279 (1954).
55. P. J. Brown and J. B. Forsyth, A neutron diffraction study of weak ferromagnetism in nickel fluoride, *J. Phys. C: Sol. St. Phys.* **14**, 5171 (1981).
56. Supplementary Material.
57. J. D. Burton and E. Y. Tsybaly, Evolution of the band alignment at polar oxide interfaces, *Phys. Rev. B* **82**, 161407(R) (2010).
58. R. Guo, L. Tao, M. Li, Z. Liu, W. Lin, G. Zhou, X. Chen, X. Yan, H. Tian, E. Y. Tsybaly, and J. Chen, Interface engineered electron and hole tunneling, *Sci. Adv.* **7**, eabf1033 (2021).